

Catalytic behavior of supported Ru nanoparticles on the (101) and (001) facets of anatase TiO₂†

Cite this: *RSC Adv.*, 2014, 4, 10834

Fei Wang, Shitong Zhang, Changming Li, Jie Liu, Shan He, Yufei Zhao, Hong Yan, Min Wei,* David G. Evans and Xue Duan

Ru/TiO₂ heterogeneous catalysts were prepared by immobilizing Ru nanoparticles onto the (101) and (001) facets of anatase TiO₂ substrate, and the influence of metal–support interactions on the catalytic behavior of Ru/TiO₂ towards CO₂ methanation was studied from the viewpoint of electronic structure. Structural investigations based on temperature-programmed reduction (TPR) and X-ray photoelectron spectroscopy (XPS) indicate that a stronger metal–support interaction occurs between Ru and (101) facet in contrast to the Ru and (001) one. This gives rise to an enhancement in CO₂ adsorption as well as spill-over hydrogen at the interface of Ru/TiO₂(101), accounting for its largely enhanced catalytic activity towards CO₂ methanation. In addition, a theoretical study based on density functional theory (DFT) calculations reveals that the Ru nanoparticles supported on the (101) plane have a relatively lower activation energy for CO dissociation (the rate-determining step), which results in their high activity toward CO₂ methanation reaction.

Received 27th November 2013

Accepted 5th February 2014

DOI: 10.1039/c3ra47076h

www.rsc.org/advances

1. Introduction

The metal–support interaction has attracted considerable attention in the area of supported heterogeneous catalysis, since the support will have significant influences on the adsorptive capacity,^{1,2} electron transfer,^{3,4} and chemical and electronic structure of the active metal.^{5–7} This will eventually affect the catalytic activity and selectivity. Recently, great efforts have been devoted to the design and fabrication of supported metal catalysts by changing the crystal structure, morphology, or particle size of supports.^{5,8–11} It has also been reported that specific exposed facets of the support play a key role in determining the metal–support interaction and the resulting catalytic behavior, because the atomic species, coordination environment and electron density of various planes are rather different.^{5,12} Although several studies have demonstrated that the exposed facet of support nanocrystals could exert profound effect on the catalytic activity and selectivity,^{13–15} the intrinsic effect of support facet on the metal–support interaction is unclear. A detailed understanding of crystal plane of supports in a heterogeneous catalysis system for the purpose of obtaining largely enhanced catalytic performance remains a challenging goal.

In recent decades, global warming from green house gases (mainly CO₂) produced by the burning of fossil fuels has

attracted increasing attention, and how to achieve the recycle of carbon has become perhaps the most complicated issue. The catalytic hydrogenation of CO₂ to give methane, known as methanation, is an efficient approach to recycle exhausted CO₂ to give a useful fuel, with potential commercial applications and environmental benefits.^{16,17} Supported ruthenium (Ru) catalysts hold a prominent position for their extremely high activity in this reaction;¹⁸ additionally, the metal–support interaction was also found to impose an essential effect on the catalytic performance. Kowalczyk *et al.* reported that for Ru catalysts supported on various substrates, the following sequence of TOFs was obtained: Ru/Al₂O₃ > Ru/MgAl₂O₄ > Ru/MgO > Ru/C.¹⁹ Several studies on this area have also confirmed the catalytic activity is strongly affected by the interaction between Ru nanoparticles and oxide supports both for CO₂ methanation and other related reactions.^{20–22} However, the influence of exposed crystal planes of support on the catalytic behavior of Ru nanoparticles, which is crucial to improve the catalytic efficiency of noble metal from the viewpoint of electronic structure, is not well-resolved.

In this work, active Ru species was respectively supported on two kinds of anatase titanium dioxide (TiO₂), *i.e.*, TiO₂ nanoparticles (NPs) with exposed (101) plane and nanosheets (NSs) with (001) facet (denoted as Ru/TiO₂(101) and Ru/TiO₂(001), respectively), and their catalysis evaluation towards CO₂ methanation was carried out to shed light on the key role of metal–support interaction. TPR results indicate that a stronger metal–support interaction was found between Ru and (101) facet relative to Ru and (001) one. XPS further shows that there is a stronger electron transfer from Ru nanoparticles to TiO₂

State Key Laboratory of Chemical Resource Engineering, Beijing University of Chemical Technology, Beijing 100029, China. E-mail: weimin@mail.buct.edu.cn; Fax: +86-10-64425385; Tel: +86-10-64412131

† Electronic supplementary information (ESI) available. See DOI: 10.1039/c3ra47076h

(101) facet compared with TiO₂ (001) facet, which results in a larger capacity of hydrogen and CO₂ adsorption as well as spill-over hydrogen at the metal–support interface of Ru/TiO₂(101), accounting for its largely enhanced catalytic activity. DFT calculations further reveal that the Ru species supported on the (101) plane have a relatively lower activation energy for the CO dissociation, leading to its high reactivity toward CO₂ methanation. This work provides a detailed understanding of metal–support interaction originating from exposed crystal plane of substrates, which can be used for the design and fabrication of supported heterogeneous catalysts with high performance.

2. Experimental section

2.1 Preparation of TiO₂ supports and Ru/TiO₂ catalysts

All the reagents were of analytical grade and used without further purification. Anatase TiO₂ nanosheets (TiO₂-NSs) with exposed (001) facet were prepared by a hydrothermal method similar to that described by Xie *et al.*²³ In a typical experiment, 25 mL of Ti(OC₄H₉)₄ and 3 mL of hydrofluoric acid solution (with a concentration of 50 wt%) were mixed in a 100 mL Teflon-lined autoclave at room temperature, followed by a hydrothermal treatment at 180 °C for 24 h. The resulting white precipitate (TiO₂-NSs) was collected, washed with ethanol, distilled water and then 0.1 mol L⁻¹ NaOH solution to eliminate the remaining fluorine, followed by drying at 80 °C for 6 h. Anatase TiO₂ nanoparticles (TiO₂-NPs) with exposed (101) facet were also prepared by a similar method except that the 3 mL of hydrofluoric acid was replaced by 3 mL of distilled water.

The Ru/TiO₂ catalysts (Ru/TiO₂(101) and Ru/TiO₂(001)) were prepared by a deposition–precipitation method. 3.0 g of TiO₂ was suspended in 80 mL of water followed by adding 0.1518 g of RuCl₃·3H₂O (2 wt%) in the suspension. The pH value of the mixture was adjusted to 8.0 by adding 1 mol L⁻¹ Na₂CO₃ solution. Afterwards, the suspension was stirred for 3 h, and then the solid was filtrated and washed thoroughly, dried in air at 60 °C for 12 h. The product was heated at a constant rate (5 °C min⁻¹) from room temperature to 300 °C in a N₂ atmosphere and held for 3 h, followed by a reduction in a H₂–N₂ mixture (2 : 3, v/v) with 100 mL min⁻¹ flow at 300 °C for 3 h.

2.2 Catalyst characterization

X-ray diffraction (XRD) patterns of samples were obtained on a Shimadzu XRD-6000 diffractometer, using Cu K α radiation (λ = 0.154 nm) at 40 kV, 30 mA, a scanning rate of 5°/min, a step size of 0.02°/s, and a 2 θ angle ranging from 15 to 70°. Elemental analysis of metal in samples was performed using a Shimadzu ICPS-7500 inductively coupled plasma emission spectrometer (ICP-ES). Transmission electron microscopy (TEM) and high-resolution TEM (HRTEM) observations were carried out on a JEOL JEM-2100 transmission electron microscope. Low-temperature N₂ adsorption–desorption isotherms of the samples were obtained on a Micromeritics ASAP 2020 sorptometer apparatus. All samples were outgassed prior to analysis at 200 °C for 12 h under 10⁻⁴ Pa vacuum. The total specific surface area was evaluated from the multipoint Brunauer–

Emmett–Teller (BET) method. X-ray photoelectron spectroscopy (XPS) measurements were performed using an ESCALAB 250 instrument (Thermo Electron) with Al K α radiation. The binding energy calibration of all spectra was referenced to the C1s signal at 284.6 eV.

Temperature programmed reduction (TPR) and temperature programmed desorption (TPD) of the samples were performed by using a Micromeritics ChemiSorb 2720 with a thermal conductivity detector (TCD). Before measurement, the sample (100 mg) placed in a quartz U-tube reactor was degassed under flowing argon at 200 °C for 2 h. For TPR, the sample was reduced in a stream of H₂–Ar (1 : 9, v/v; 40 mL min⁻¹ total flow) with a heating rate of 10 °C min⁻¹ up to 400 °C. For TPD, the sample (300 mg) was reduced under the same conditions mentioned above, and then cooled to room temperature. Subsequently, TPD measurement was carried out in a stream of argon with a rate of 40 mL min⁻¹ and a temperature ramp of 10 °C min⁻¹.

2.3 Evaluation of catalytic performance

The catalytic evaluation of the supported Ru catalysts for CO₂ methanation was carried out in a quartz tube reactor (8 mm in diameter) at atmospheric pressure. Brooks mass flow controllers were used to control the gas flow rate. In order to eliminate temperature and concentration gradients, 1.0 g of the catalyst was mixed with 1 mL of inert quartz sand (40 to 60 mesh) and then packed into the reactor. The reactor temperature was controlled by three thermocouples (located near the entrance, at the middle, and near the exit of the bed). After the catalyst pretreatment, the reaction gas mixture consisting of CO₂ (15%, v/v), H₂ (60%, v/v) and Ar (25%, v/v) at 40 standard cubic centimeters per minute (sccm) total flow rate was introduced into the reactor, and the CO₂ conversion was measured over the temperature range 150–350 °C. The product gas stream was analyzed on line by gas chromatography (GC, Shimadzu, 2014C) equipped with a thermal conductivity detector (TCD). The CO₂ conversion was calculated based on the CO₂, H₂ and CH₄ mole fractions in the products.

2.4 Computational methods

Periodic density functional theory (DFT) calculations were performed using the DMol³ code. The (101) and (001) surface were simulated by a (3 × 3) slab, with a thickness of four titanium layers. According to the previously reported work, the (3 × 3) slab is large enough to reduce the interactions between neighboring images and allows the interfacial strain energy to be fully released. In addition, a vacuum space of 15.0 Å above the surface was employed to eliminate the interaction between two neighboring images along the vertical direction. All the atoms were fully relaxed during the geometric optimization. The generalized gradient approximation with the Perdew–Burke–Ernzerhof functional, together with effective core potentials was utilized. The basis set was specified as the double-numerical basis with polarization functions. The convergence criteria for structure optimizations were based on the following: (1) an energy tolerance of 2.0 × 10⁻⁵ Ha per atom; (2) a maximum

force tolerance of 4.0×10^{-3} Ha/Å; (3) a maximum displacement tolerance of 4.0×10^{-3} Å. *k*-space was sampled by the gamma point. The Ru₁₃ cluster was used for simulation in this work, which has been proved to be valid in studying Ru-support interaction previously.²⁴ This cluster size can serve as a useful model for atoms with low coordination number (*e.g.*, those on corners and edges of nanoparticles), which are expected to show high catalytic activity. The adsorption energy (E_{ads}) of species adsorbed on the Ru₁₃/TiO₂ surface was calculated from the energy difference between the optimized surface containing the adsorbate ($E_{\text{surface+adsorbate}}$) and the optimized clean surface with the adsorbate molecule optimized in gas state ($E_{\text{surface}} + E_{\text{adsorbate}}$), as shown in the following equation:

$$E_{\text{ads}} = E_{\text{surface+adsorbate}} - (E_{\text{surface}} + E_{\text{adsorbate}}) \quad (1)$$

3. Results and discussion

3.1 Structural and morphological study of the catalysts

The morphology of the catalyst supports revealed by TEM and HRTEM is shown in Fig. 1. TiO₂-NSs show a typical sheet-like morphology with the lateral particle size of 60–100 nm (Fig. 1A); a well-defined truncated bipyramidal structure was displayed by the HRTEM image (Fig. 1B), with a lattice spacing of ~ 0.235 nm parallel to the top and bottom facets. This corresponds to the (001) plane of anatase TiO₂, which indicates the top and bottom facets of the nanosheets are (001) planes (Fig. 1C). By comparison, TEM images of TiO₂-NPs (Fig. 1D and E) show that the lattice spacing parallel to the side face of the truncated bipyramid is ~ 0.35 nm, corresponding to the (101) plane of anatase TiO₂. On the basis of the structural information, the percentage of exposed (001) facet for the TiO₂-NSs is $\sim 75\%$; while the percentage of exposed (101) facet for the TiO₂-NPs is large than 90%.

Fig. 2 illustrates the XRD patterns of the two TiO₂ substrates and resulting Ru/TiO₂ catalysts. All the diffraction peaks match well with the crystal structure of the anatase TiO₂ phase (JCPDS no. 21-1272, space group: *I4₁/amd* (141)).²⁵ Specially, TiO₂-NSs

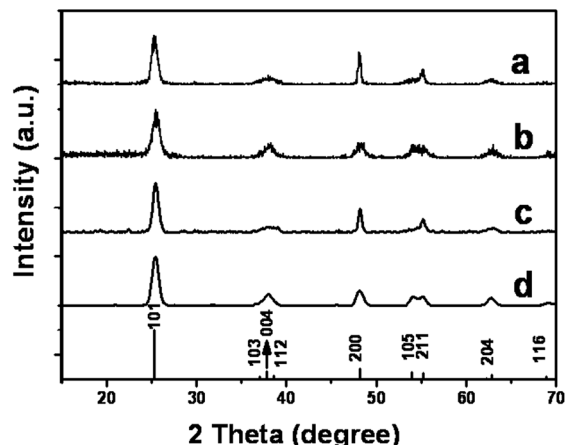


Fig. 2 XRD patterns of the (a) TiO₂-NSs, (b) TiO₂-NPs, (c) Ru/TiO₂(001) and (d) Ru/TiO₂(101).

(curve a) exhibit relatively stronger (200) reflection and weaker (004) reflection in comparison with TiO₂ NPs (curve b), indicating the predominant exposure of (001) plane. This agrees well with the HRTEM results above and previous reports.²⁶ Moreover, no obvious change in the XRD patterns after loading Ru (curve c and d) was observed, suggesting the maintenance of the structure and morphology of these two TiO₂ substrates. It should be noted that Ru species shows no characteristic XRD reflection, probably owing to the high dispersion of Ru NPs with rather small particle size (below the detection limit of XRD).

Fig. 3 shows the TEM and HRTEM images of the two Ru/TiO₂ catalysts. It is observed that the original morphology of TiO₂ substrate basically remains, and Ru nanoparticles are highly dispersed throughout the support. The histogram of the particle size distribution for Ru/TiO₂(001) (Fig. 3C), which is calculated from more than 200 nanoparticles, presents a narrow distribution. The mean particle size was calculated to be ~ 1.5 nm. The Ru/TiO₂(101) sample shows a similar dispersion of Ru nanoparticles with a mean particle diameter of ~ 1.6 nm (Fig. 3D).

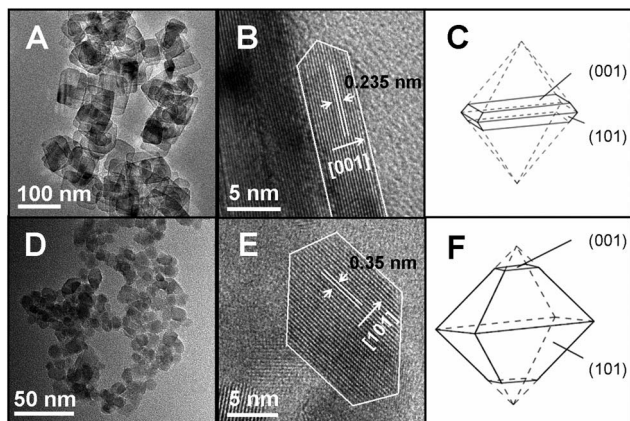


Fig. 1 (A–C) TEM, HRTEM image and the schematic illustration of TiO₂-NSs with exposed (001) facet; (D–F) TEM, HRTEM image and the schematic illustration of TiO₂-NPs with exposed (101) facet.

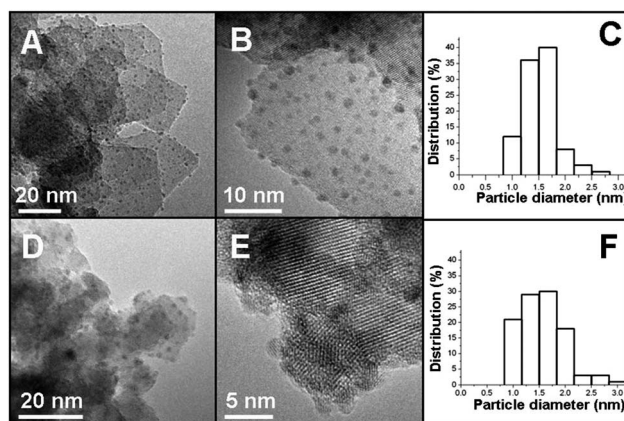


Fig. 3 (A and B) TEM images and (C) the histogram of the particle size distribution of Ru/TiO₂(001); (D and E) TEM images and (F) the histogram of the particle size distribution of Ru/TiO₂(101).

As shown in Table 1, the BET specific surface area decreases slightly from $96 \text{ m}^2 \text{ g}^{-1}$ ($\text{TiO}_2\text{-NSs}$) to $72 \text{ m}^2 \text{ g}^{-1}$ ($\text{Ru}/\text{TiO}_2(001)$) with the deposition of Ru nanoparticles; a similar trend was found for the $\text{Ru}/\text{TiO}_2(101)$ sample (decreases from 141 to $115 \text{ m}^2 \text{ g}^{-1}$). This is possibly attributed to partial agglomeration of TiO_2 support during the wet impregnation process for the deposition of Ru species. Elemental analysis by ICP-AES reveals the Ru contents are 1.69% and 1.66% in the two catalyst samples (Table 1), which are slightly lower than the nominal content (2%).

3.2 Catalytic activity

The catalytic behavior of the $\text{Ru}/\text{TiO}_2(001)$ and $\text{Ru}/\text{TiO}_2(101)$ samples was evaluated using CO_2 methanation as a probe reaction. Fig. 4A shows CO_2 conversion vs. reaction temperature over the two catalysts with a reaction-gas feed rate of $40 \text{ mL g}^{-1} \text{ s}^{-1}$. For the sample of $\text{Ru}/\text{TiO}_2(001)$, the CO_2 conversion increases along with the increase of temperature and reaches to the maximum value of 91% at $350 \text{ }^\circ\text{C}$. In the case of $\text{Ru}/\text{TiO}_2(101)$ however, the maximum conversion of 98% was obtained at $255 \text{ }^\circ\text{C}$, demonstrating an excellent high activity at low temperature. It should be noted that both $\text{Ru}/\text{TiO}_2(001)$ and $\text{Ru}/\text{TiO}_2(101)$ have very satisfactory selectivity towards CH_4 (>99%) over the whole temperature range. The turnover frequency (TOF) of the two catalysts was evaluated at low reaction temperature ($150 \text{ }^\circ\text{C}$), low CO_2 conversion (<15%) and high CO_2 weight hourly space velocity (WHSV: $360 \text{ mL g}_{\text{cat}}^{-1} \text{ h}^{-1}$), so as to minimize the effect of transport and water inhibition. The TOF values were calculated to be $4.51 \times 10^{-3} \text{ s}^{-1}$ and $2.57 \times 10^{-3} \text{ s}^{-1}$ for $\text{Ru}/\text{TiO}_2(101)$ and $\text{Ru}/\text{TiO}_2(001)$, indicating a largely enhanced catalytic activity of the former catalyst. The activation energy (E_a) values were also measured by dynamical experiments (shown in Fig. S1†). According to the Arrhenius equation, the E_a of CH_4 formation on $\text{Ru}/\text{TiO}_2(101)$ (65.9 kJ mol^{-1}) is lower than that on $\text{Ru}/\text{TiO}_2(001)$ (77.4 kJ mol^{-1}), which agrees with the TOF results.

The long-term catalytic stability of the two samples was also investigated. As shown in Fig. 4B, the $\text{Ru}/\text{TiO}_2(101)$ exhibits a stable conversion (95%) at $325 \text{ }^\circ\text{C}$ for 50 h, with no obvious decrease in its activity (curve a), indicating a sufficient stability for long-term employment. For the $\text{Ru}/\text{TiO}_2(001)$ sample however (curve b), a continuous decrease in the CO_2 conversion (from 92% to 87%) at $325 \text{ }^\circ\text{C}$ was observed with a reaction duration of 50 h. Since the Ru loading and particle size are

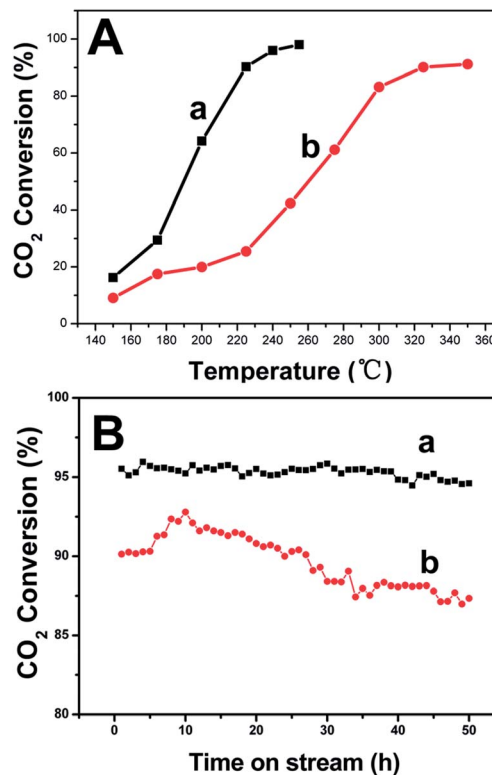


Fig. 4 (A) The CO_2 conversion at steady state as a function of reaction temperature: (a) $\text{Ru}/\text{TiO}_2(101)$, (b) $\text{Ru}/\text{TiO}_2(001)$; (B) time-on-stream analysis for (a) $\text{Ru}/\text{TiO}_2(101)$ and (b) $\text{Ru}/\text{TiO}_2(001)$ at $325 \text{ }^\circ\text{C}$.

rather close for these two Ru/TiO_2 catalysts, the obvious difference in catalytic performance can be attributed to the support effect originating from the exposed facet, which will be discussed in detail in the next section.

3.3 Influences of metal-support interaction on catalytic performance

In order to give an insight into the metal-support interaction in these Ru/TiO_2 catalysts, TPR was carried out to probe the reducibility of supported Ru catalysts. Fig. 5 shows the TPR profiles of two $\text{RuO}_2/\text{TiO}_2$ catalysts, with pristine RuO_2 as a reference sample which was prepared by similar DP method without addition of any support. Only one reduction peak at $188 \text{ }^\circ\text{C}$ was observed for the pristine RuO_2 (curve c), corresponding to the reduction process of Ru^{4+} to Ru^0 .²⁷ In the case of the immobilized RuO_2 , both the $\text{RuO}_2/\text{TiO}_2(101)$ and $\text{RuO}_2/\text{TiO}_2(001)$ show significantly increased reduction temperature, *i.e.*, at 276 and $233 \text{ }^\circ\text{C}$, indicating that TiO_2 support hinders the reduction process of RuO_2 . The $\text{RuO}_2/\text{TiO}_2(101)$ sample displays a much higher temperature shift in comparison with $\text{RuO}_2/\text{TiO}_2(001)$ one, implying a stronger interaction between Ru species and the (101) facet. Moreover, a larger amount of H_2 consumption was found in the $\text{RuO}_2/\text{TiO}_2(101)$ catalyst. The values of H/Ru ratio are 23.3 and 11.0 for the $\text{RuO}_2/\text{TiO}_2(101)$ and $\text{RuO}_2/\text{TiO}_2(001)$, respectively, implying that the TiO_2 support in the former system shows a stronger extent of reduction *via* the spillover mechanism.²⁸

Table 1 BET surface area and Ru loading for the supported catalysts

Samples	$S_{\text{BET}}^a/\text{m}^2 \text{ g}^{-1}$	Ru loading ^b /wt%	TOF _{CH₄} ^c at $150 \text{ }^\circ\text{C} \text{ s}^{-1}$
$\text{TiO}_2\text{-NSs}$	96	—	—
$\text{TiO}_2\text{-NPs}$	141	—	—
$\text{Ru}/\text{TiO}_2(001)$	72	1.69	2.57×10^{-3}
$\text{Ru}/\text{TiO}_2(101)$	115	1.66	4.51×10^{-3}

^a BET surface area. ^b Determined by ICP-AES. ^c Turnover frequency of CO_2 hydrogenation, which was given as the overall rate of CO_2 conversion normalized by the number of active sites over the specified time.

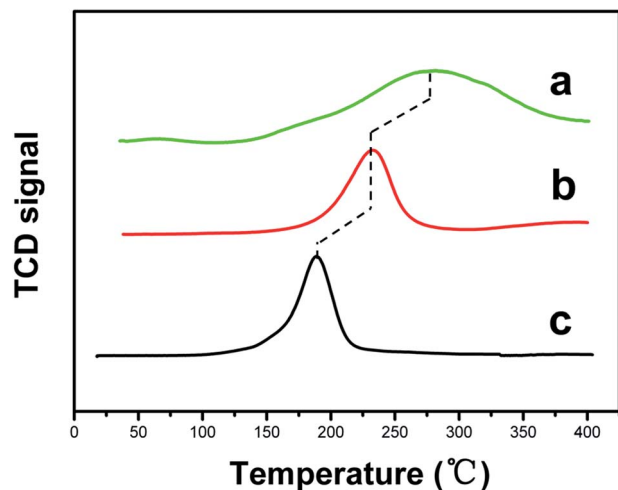


Fig. 5 H₂-TPR profiles of (a) RuO₂/TiO₂(101), (b) RuO₂/TiO₂(001) and (c) pristine RuO₂.

Fig. 6 shows the XPS spectra of Ru 3d peak of the two supported Ru catalysts as well as pristine Ru sample. The peak at ~ 280.1 for pristine Ru sample (Fig. 6c) can be assigned to Ru 3d_{5/2}, indicative of metallic Ru. Similarly, the peaks of Ru 3d_{5/2} for Ru/TiO₂(101) and Ru/TiO₂(001) are observed at ~ 280.5 and 280.1 eV, respectively. Interestingly, the binding energy of Ru 3d for Ru/TiO₂(101) exhibits a positive shift compared with that of pristine Ru and Ru/TiO₂(001), which can be attributed to the modification in the electronic structure of Ru nanoparticles. Such a positive shift indicates an obvious electron transfer from metallic Ru to TiO₂ (101) facet.^{27,29} The positive polarity of Ru species may have influence on the binding energy of the adsorbates and their dissociation process, which will affect the catalytic property.^{30,31}

Hydrogen can be adsorbed in several ways on supported catalysts. TPD has been found to be quite useful for characterizing catalysts by fingerprint spectra and for determining metal surface areas, binding energies and binding states of adsorbed

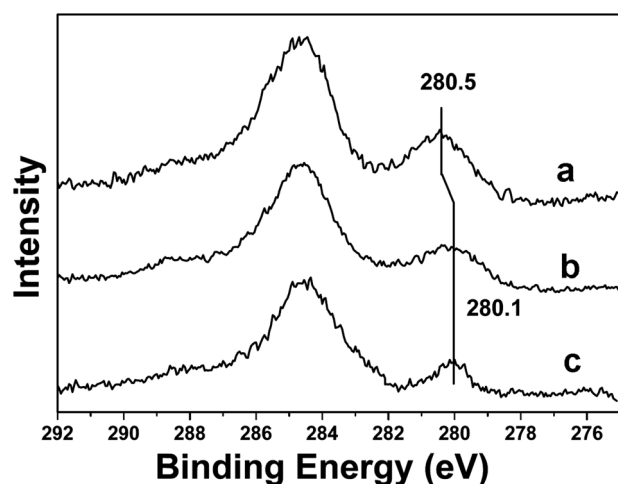


Fig. 6 XPS profiles of Ru: (a) Ru/TiO₂(101), (b) Ru/TiO₂(001), (c) pristine Ru.

molecules.³² Fig. 7A displays the H₂-TPD profiles obtained over the two Ru/TiO₂ catalysts. It is observed that hydrogen desorbs from the Ru/TiO₂(101) sample (curve a) exhibiting three peaks centered at ~ 90 , 285 and 480 °C, respectively. According to the results of previous studies,^{33–35} the low temperature peak (LT, 90 °C) is due to hydrogen chemisorbed at the surface of Ru nanoparticles; the medium temperature peak (MT, 285 °C) is assigned to hydrogen adsorbed at the metal-support interface; the high temperature (HT, 480 °C) hydrogen desorption can be attributed to spilt-over hydrogen or strongly chemisorbed hydrogen. In the case of Ru/TiO₂(001) however, its TPD profile is characterized by one main peak located at ~ 140 °C (Fig. 7A, curve b), which can be possibly attributed to the hydrogen chemisorbed at the surface of Ru nanoparticles. The absence of MT and HT peak in the Ru/TiO₂(001) system excludes the hydrogen adsorbed at the metal-support interface and spillover hydrogen, suggesting a weak synergistic effect between the metallic Ru and (001) facet of TiO₂.

Fig. 7B displays the CO₂-TPD profiles of the two TiO₂ supports and the resulting two Ru/TiO₂ catalysts. TiO₂-NPs and TiO₂-NSs show rather similar behavior (curve c and curve d), *i.e.*, only one peak occurs at ~ 460 °C. In order to confirm the origin of this peak, we performed the CO₂-TPD of the TiO₂-NPs after a

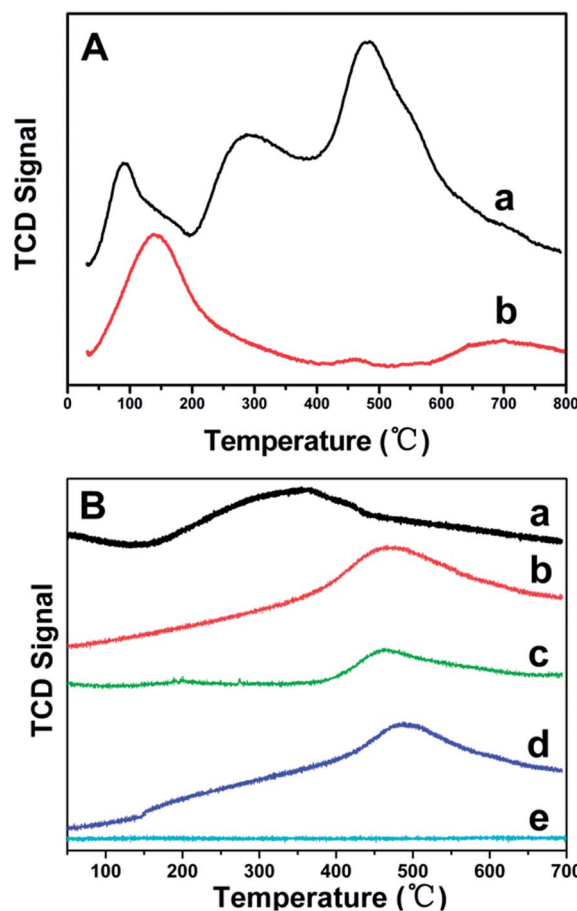


Fig. 7 (A) H₂-TPD profiles of (a) Ru/TiO₂(101), (b) Ru/TiO₂(001); (B) CO₂-TPD profiles of (a) Ru/TiO₂(101), (b) Ru/TiO₂(001), (c) TiO₂-NPs, (d) Ru/TiO₂-NSs, (e) TiO₂-NPs-600.

heat treatment at 600 °C for 1 h in Ar atmosphere (denoted as TiO₂-NPs-600, Fig. 7B, curve e), in comparison with the TiO₂-NPs without heat treatment (Fig. 7B, curve c). The peak at ~460 °C disappeared for TiO₂-NPs-600, which indicates that this peak is not due to the desorption of CO₂, but most probably due to the dehydroxylation of the support. The Ru/TiO₂(001) sample (curve b) shows almost the same feature with the two supports, indicating that the immobilization of Ru nanoparticles does not contribute to the CO₂ adsorption in this system. Interestingly, the Ru/TiO₂(101) sample exhibits obviously different character. Besides a shoulder peak (~460 °C) similar to that of the TiO₂-NPs substrate, a strong and broad peak for CO₂ desorption was observed at ~320 °C, which can be attributed to CO₂ that adsorbs at the surface of Ru and/or the Ru–TiO₂ interface.³⁶ The results demonstrate that a stronger adsorption of reactants (both H and CO₂) occurs on the surface of Ru/TiO₂(101) catalyst in contrast to the Ru/TiO₂(001) one, resulting from the stronger metal–support interaction between Ru and (101) facet of anatase TiO₂.

For the methanation of CO₂, there is still no consensus on the reaction mechanism. One important proposal involves the conversion of CO₂ to CO prior to methanation, followed by the same mechanism as CO methanation, in which the rate-determining step is the formation of surface carbon in CO dissociation.³⁷ To gain a further insight into the catalytic activity of the present catalysts, DFT calculations were carried out to elucidate the structure–activity correlation. In this work, we optimized the structure of Ru₁₃ cluster and subsequently supported them on (101) and (001) surface of TiO₂, respectively. This cluster can serve as a suitable model for atoms with low coordination number (*e.g.*, those on corners and edges of nanoparticles), which is expected to show high catalytic activity. The Hirshfeld charge results show that Ru₁₃ is positively charged, indicating the electron transfer from Ru₁₃ to TiO₂ (Fig. S2†). The total Hirshfeld charge of Ru₁₃ in Ru₁₃/TiO₂(101) is 0.98e, 0.13e higher than that in Ru₁₃/TiO₂(001), which is in accordance with the XPS results. In addition, the electronic interaction is mainly localized in the Ru atoms direct contacting with the support; while those in noncontacting layers, are less affected by the electronic interaction. Subsequently, the direct CO dissociation (the rate-determining step) on these two models was studied. Five different adsorption geometries of CO were calculated, and the most stable one was chosen for further calculations. According to the calculated adsorption energies, it is suggested that CO prefers to bind at the Ru–TiO₂ interface both in Ru₁₃/TiO₂(101) and Ru₁₃/TiO₂(001) system (Fig. 8). This adsorption phenomenon has also been observed by Panagiotopoulou previously.³⁸ The adsorption energy of CO on Ru₁₃/TiO₂(101) is –1.71 eV, lower than that on Ru₁₃/TiO₂(001) by 0.65 eV, indicating that the CO molecule binds more strongly with Ru₁₃/TiO₂(101). Moreover, the adsorption energy of CO on the pristine Ru₁₃ cluster is –0.08 eV, much higher than on the supported Ru₁₃ clusters (–1.71 and –1.06 eV, respectively), which indicates that CO binds more strongly on the supported ones. It's known that the energy of CO adsorption is highly sensitive to the electronic state of the adsorption site,³⁹ and the positively charged Ru atoms are desirable for the adsorption of CO.

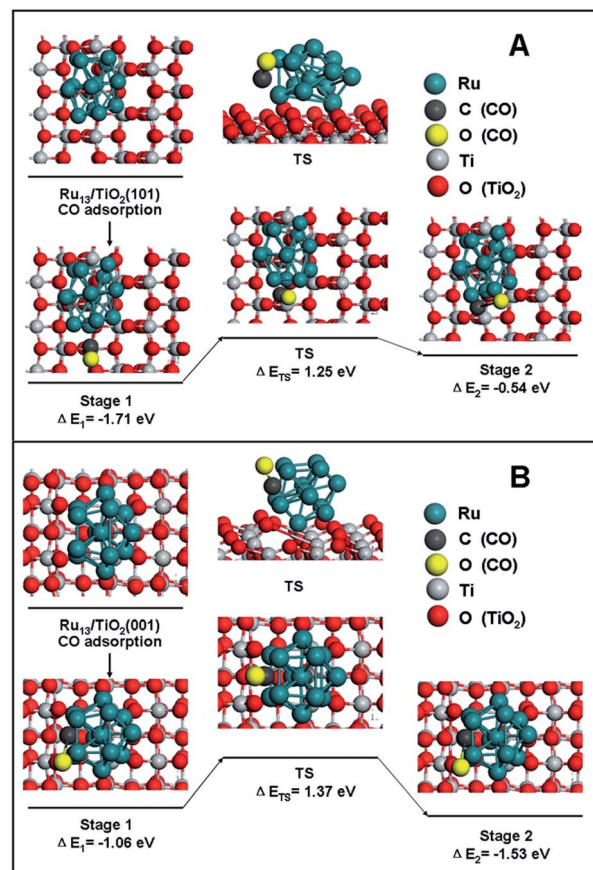


Fig. 8 CO dissociation on: (A) Ru₁₃/TiO₂(101) and (B) Ru₁₃/TiO₂(001), respectively.

Furthermore, the TPD results above confirm that both H and CO₂ adsorb more strongly on the Ru₁₃/TiO₂(101) system. It is therefore deduced that the stronger electron transfer from the Ru₁₃ cluster to TiO₂ (101) leads to a better stability of chemical species on this catalyst. For this reason, the transition-state (TS) was stabilized considerably for the Ru₁₃/TiO₂(101) system, in comparison with the Ru₁₃/TiO₂(001) one, rendering a much lower CO dissociation barrier for Ru₁₃/TiO₂(101) system (1.25 eV) than that for Ru₁₃/TiO₂(001) one (1.37 eV). This accounts for the higher activity of Ru₁₃/TiO₂(101) catalyst toward CO₂ methanation than that of Ru₁₃/TiO₂(001).

4. Conclusions

Ru nanoparticles supported on the (101) facet of anatase TiO₂ exhibit significantly higher activity for the catalytic hydrogenation of CO₂ to methane than that on the (001) facet. Structural investigations based on TPR and XPS technique give direct evidence that a stronger metal–support interaction occurs between Ru and (101) facet in contrast to Ru and (001) one. This gives rise to an enhancement in reactants adsorption (both H and CO₂) at the interface of Ru/TiO₂(101), accounting for the observed surprisingly high reactivity and good stability of the Ru/TiO₂(101) catalyst. In addition, a theoretical study based on DFT calculations further confirms the stronger electron transfer

from Ru cluster to TiO₂ (101) facet than to TiO₂ (001) one; the Ru species supported on the (101) plane possesses a relatively lower activation energy for the CO dissociation, resulting in its highly catalytic activity toward CO₂ methanation reaction. This work provides a fundamental understanding of the metal-support interaction originating from exposed facet of support. It is expected that this strategy can be extended to the design and fabrication of other supported metal catalysts with significantly enhanced behavior in heterogeneous catalysis.

Acknowledgements

This work was supported by the 973 Program (Grant no. 2011CBA00504), the National Natural Science Foundation of China (NSFC), the Scientific Fund from Beijing Municipal Commission of Education (20111001002) and the Fundamental Research Funds for the Central Universities (ZD 1303). M. Wei particularly appreciates the financial aid from the China National Funds for Distinguished Young Scientists of the NSFC.

Notes and references

- 1 S. J. Tauster, S. C. Fung and R. L. Garten, *J. Am. Chem. Soc.*, 1978, **100**, 170–175.
- 2 Z. H. Qin, M. Lewandowski, Y. N. Sun, S. Shaikhutdinov and H. J. Freund, *J. Phys. Chem. C*, 2008, **112**, 10209–10213.
- 3 X. Y. Liu, M. H. Liu, Y. C. Luo, C. Y. Mou, S. D. Lin, H. K. Cheng, J. M. Chen, J. F. Lee and T. S. Lin, *J. Am. Chem. Soc.*, 2012, **134**, 10251–10258.
- 4 K. Bramhaiah and N. S. John, *RSC Adv.*, 2013, **3**, 7765–7773.
- 5 J. Li, J. L. Chen, W. Song, J. L. Liu and W. J. Shen, *Appl. Catal., A*, 2008, **334**, 321–329.
- 6 Q. Shen, L. Li, C. He, X. Zhang, Z. Hao and Z. Xu, *Asia-Pac. J. Chem. Eng.*, 2012, **7**, 502–509.
- 7 A. S. Ivanova, E. M. Slavinskaya, R. V. Gulyaev, V. I. Zaikovskii, O. A. Stonkus, I. G. Danilova, L. M. Plyasova, I. A. Polukhina and A. I. Boronin, *Appl. Catal., B*, 2010, **97**, 57–71.
- 8 A. D. Moore, S. M. Holmes and E. P. L. Roberts, *RSC Adv.*, 2012, **2**, 1669–1674.
- 9 C. J. Miller and D. O'Hare, *Chem. Commun.*, 2004, 1710–1711.
- 10 H. Liu, P. Cheung and E. Iglesia, *J. Catal.*, 2003, **217**, 222–232.
- 11 X. Gao, C. Chen, S. Ren, J. Zhang and D. Su, *Chin. J. Catal.*, 2012, **33**, 1069–1074.
- 12 K. B. Zhou and Y. D. Li, *Angew. Chem., Int. Ed.*, 2011, **50**, 2–14.
- 13 R. Si and M. F. Stephanopoulos, *Angew. Chem., Int. Ed.*, 2008, **47**, 2884–2887.
- 14 L. J. Liu, Z. J. Yao, Y. Deng, F. Gao, B. Liu and L. Dong, *ChemCatChem*, 2011, **3**, 978–989.
- 15 J. F. Liu, W. Chen, X. W. Liu, K. B. Zhou and Y. D. Li, *Nano Res.*, 2008, **1**, 46–55.
- 16 W. Wang, S. P. Wang, X. B. Ma and J. L. Gong, *Chem. Soc. Rev.*, 2011, **40**, 3703–3727.
- 17 J. N. Park and E. W. Mcfarl, *J. Catal.*, 2009, **266**, 92–97.
- 18 P. Panagiotopoulou, D. I. Kondarides and X. E. Verykios, *Appl. Catal., A*, 2008, **344**, 45–54.
- 19 Z. Kowalczyk, K. Stołeczki, W. Raróg-Pilecka, E. Miśkiewicz, E. Wilczkowska and Z. Karpiński, *Appl. Catal., A*, 2008, **342**, 35–39.
- 20 E. S. Vasiliadou, E. Heracleous, I. A. Vasalos and A. A. Lemonidou, *Appl. Catal., B*, 2009, **92**, 90–99.
- 21 L. Wang, J. Chen, L. Ge, V. Rudolph and Z. Zhu, *RSC Adv.*, 2013, **3**, 12641–12647.
- 22 Y. H. Kim and E. D. Park, *Appl. Catal., B*, 2010, **96**, 41–50.
- 23 X. G. Han, Q. Kuang, M. S. Jin, Z. X. Xie and L. S. Zheng, *J. Am. Chem. Soc.*, 2009, **131**, 3152–3153.
- 24 H. Gao and J. Zhao, *J. Chem. Phys.*, 2010, **132**, 234704.
- 25 Z. Tan, K. Sato, S. Takami, C. Numako, M. Umetsu, K. Soga, M. Nakayama, R. Sasaki, T. Tanaka, C. Ogino, A. Kondo, K. Yamamoto, T. Hashishin and S. Ohara, *RSC Adv.*, 2013, **3**, 19268–19271.
- 26 L. Qi, J. Yu and M. Jaroniec, *Phys. Chem. Chem. Phys.*, 2011, **13**, 8915–8923.
- 27 E. V. Ramos-Fernández, J. Silvestre-Albero, A. Sepúlveda-Escribano and F. Rodríguez-Reinoso, *Appl. Catal., A*, 2010, **374**, 221–227.
- 28 C. D. Leitenburg, A. Trovarelli and J. Kašpar, *J. Catal.*, 1997, **166**, 98–107.
- 29 C. M. Li, S. T. Zhang, B. S. Zhang, D. S. Su, S. He, Y. F. Zhao, J. Liu, F. Wang, M. Wei, D. G. Evans and X. Duan, *J. Mater. Chem. A*, 2013, **1**, 2461–2467.
- 30 R. L. Martins, M. A. S. Baldanza and M. Schmal, *J. Phys. Chem. B*, 2001, **105**, 10303–10307.
- 31 C. Elmasides, D. I. Kondarides, S. G. Neophytides and X. E. Verykios, *J. Catal.*, 2001, **198**, 195–207.
- 32 P. Ferreira-Aparicio, A. Guerrero-Ruiz and I. Rodríguez-Ramos, *J. Chem. Soc., Faraday Trans.*, 1997, **93**, 3563–3567.
- 33 P. Panagiotopoulou and D. I. Kondarides, *J. Catal.*, 2009, **267**, 57–66.
- 34 H. Lin and Y. Chen, *Thermochim. Acta*, 2004, **419**, 283–290.
- 35 P. Panagiotopoulou and D. I. Kondarides, *J. Catal.*, 2008, **260**, 141–149.
- 36 Y. Zhou, S. Wang, M. Xiao, D. Han, Y. Lu and Y. Meng, *RSC Adv.*, 2012, **2**, 6831–6837.
- 37 S. J. Choe, H. J. Kang, S. J. Kim, S. B. Park, D. H. Park and D. S. Huh, *Bull. Korean Chem. Soc.*, 2005, **26**, 1682–1688.
- 38 P. Panagiotopoulou, D. I. Kondarides and X. E. Verykios, *J. Phys. Chem. C*, 2011, **115**, 1220–1230.
- 39 H. Y. Kim, H. M. Lee and G. Henkelman, *J. Am. Chem. Soc.*, 2012, **134**, 1560–1570.